Supplement of Atmos. Chem. Phys., 25, 1449–1476, 2025
https://doi.org/10.5194/acp-25-1449-2025-supplement

Atmospheric Chemistry and Physics
Open Access
EGU

Supplement of

Reactive nitrogen in and around the northeastern and mid-Atlantic US: sources, sinks, and connections with ozone

Min Huang et al.

Correspondence to: Min Huang (minhuang@umd.edu)

Table S1: Percent areas under all drought conditions (D0 to D4, representing abnormally dry to exceptional drought) for various eastern US states, based on the North American Drought Monitor. Highest values for the individual states are highlighted in red (data source: https://droughtmonitor.unl.edu/NADM/Statistics.aspx, last access: 12 July 2024). Drought Monitor products are developed based on many sources of information by rotating authors. They are designed to indicate various drought types.

This table complements satellite surface soil moisture and precipitation maps (Figs. 4a and S3, not directly used to develop the Drought Monitor products) to indicate the interannual variability in drought conditions. For example, all these sources suggest that from 2018 to 2023, drought conditions in Virginia gradually expanded/intensified, while fluctuated strongly in the New England region, largely driven by precipitation variability.

US States	2018 MJJ	2019 MJJ	2020 MJJ	2022 MJJ	2023 MJJ	Standard Deviation
Virginia (VA)	1.42	4.80	14.60	19.33	**25.73**	10.07
North Carolina (NC)	6.10	33.95	3.20	**60.35**	6.57	24.79
West Virginia (WV)	0.00	0.00	19.43	4.70	**43.12**	18.40
Pennsylvania (PA)	0.00	0.00	25.29	15.34	**70.76**	29.15
Ohio (OH)	3.80	0.00	33.90	5.65	**51.43**	22.60
Michigan (MI)	30.52	4.01	19.83	27.00	**55.83**	18.86
Maryland (MD)	0.00	0.00	15.17	5.83	**62.55**	26.36
Delaware (DE)	0.00	0.00	15.60	3.49	**18.30**	8.81
New Jersey (NJ)	0.00	0.00	10.02	35.57	**40.68**	19.57
New York (NY)	33.30	0.00	**48.39**	22.79	38.17	18.42
Connecticut (CT)	13.32	0.00	53.45	**66.22**	34.08	27.38
Rhode Island (RI)	12.34	0.00	32.85	**94.54**	3.38	39.00
Massachusetts (MA)	30.75	0.00	67.49	**88.03**	9.05	37.75
Vermont (VT)	60.84	0.00	**64.72**	5.93	47.45	30.71
New Hampshire (NH)	66.08	0.00	**70.39**	69.48	5.93	36.07
Maine (ME)	29.43	0.00	**65.11**	47.99	17.50	25.46

Table S2: Evaluation of the modeled mean wet deposition (dep) fluxes and speciated aerosols with observations from surface networks. The evaluation of chemicals and chemical fluxes is only performed for sites with <10% missing/invalid data and the numbers of sites are indicated in parentheses. Observation data were last retrieved on 12 July 2024. Figs. S11–14 include the maps of these variables as well as AQS speciated fine aerosol observations.

Variable [Unit]	Data	2018 MJJ	2019 MJJ	2020 MJJ	2022 MJJ	2023 MJJ
NO_3 wet dep [kgN $ha^{-1}a^{-1}$]	weekly NADP/NTN[a]	2.06 (12)	2.60 (25)	1.77 (15)	2.00 (20)	2.01 (7)
	model	1.26	1.42	0.72	1.14	0.79
NH_4 wet dep [kgN $ha^{-1}a^{-1}$]	weekly NADP/NTN	2.79 (13)	4.63 (25)	4.15 (15)	3.73 (20)	2.41 (7)
	model	1.23	1.52	1.20	1.43	1.35
SO_4 wet dep [kgS $ha^{-1}a^{-1}$]	weekly NADP/NTN	1.76 (12)	2.20 (25)	1.56 (15)	1.65 (20)	1.60 (7)
	model	1.84	2.27	1.21	1.73	1.31
Precipitation [mm h^{-1}]	weekly NADP/NTN	0.17 (13)	0.19 (25)	0.16 (15)	0.16 (20)	0.2 (7)
	model	0.17	0.17	0.13	0.17	0.17
NO_3 [µg m^{-3}][d]	weekly CASTNET[b]	0.29 (35)	0.23 (36)	0.24 (38)	0.31 (30)	0.27 (31)
	model	0.96	0.89	0.83	0.78	0.89
NH_4 [µg m^{-3}]	weekly CASTNET	0.38 (35)	0.37 (36)	0.31 (38)	0.32 (30)	0.37 (31)
	model	0.64	0.55	0.51	0.49	0.52
SO_4 [µg m^{-3}][d]	weekly CASTNET	1.11 (35)	1.04 (36)	0.90 (38)	0.97 (30)	0.94 (31)
	model	1.16	0.98	0.90	0.87	0.85
HNO_3 [µg m^{-3}]	weekly CASTNET	0.72 (35)	0.64 (36)	0.60 (38)	0.66 (30)	0.65 (31)
	model	0.77	0.68	0.60	0.66	0.71
NH_3 [µg m^{-3}]	biweekly NADP/AMoN[c]	1.52 (26)	4.52 (1)	1.62 (22)	2.32 (10)	2.07 (5)
	model	1.21	1.19	1.44	2.33	1.72

[a]National Atmospheric Deposition Program (NADP) National Trends Network (NTN): https://nadp.slh.wisc.edu/networks/national-trends-network
[b]Clean Air Status and Trends Network (CASTNET): https://www.epa.gov/castnet/download-data
[c]NADP Ammonia Monitoring Network (AMoN): https://nadp.slh.wisc.edu/networks/ammonia-monitoring-network
[d]Hand et al. (2024) reported ~10% $year^{-1}$ of downward SO_4 trends and slower NO_3 decreasing trends in spring/summer 2000–2021 based on observations from the Interagency Monitoring of Protected Visual Environments network for the Northeast US, which are similar to the results here.

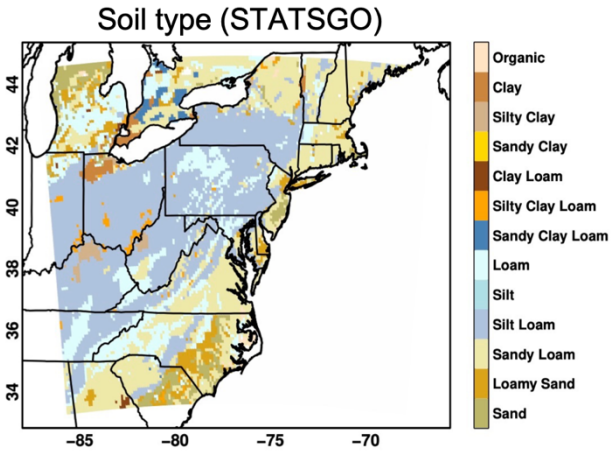

Figure S1: Grid-dominant soil type based on the State Soil Geographic (STATSGO) dataset used in all model simulations.

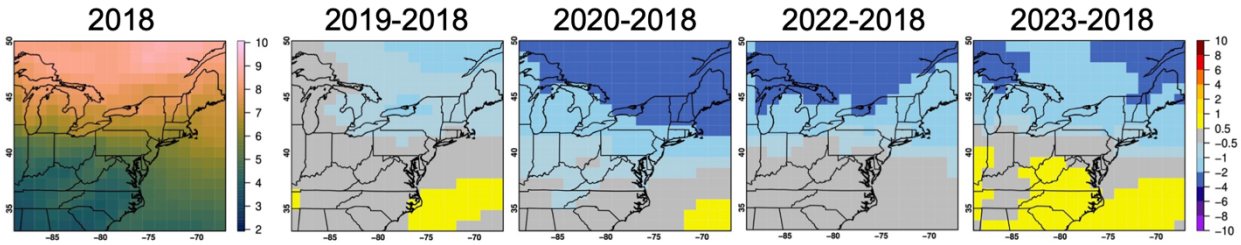

Figure S2: Stratospheric influences on MJJ surface-level O_3 and their interannual differences (all in ppbv), based on WRF-Chem's chemical boundary condition models' stratospheric O_3 tracer.

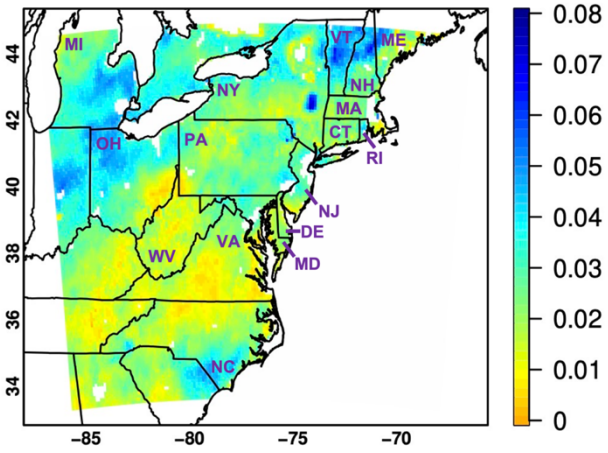

Fig. S3: Standard deviation of SMAP morning-time surface soil moisture ($m^3\ m^{-3}$) for MJJ 2018–2023, on WRF-Chem grids. State names (full definitions in Table S1) are marked in purple.

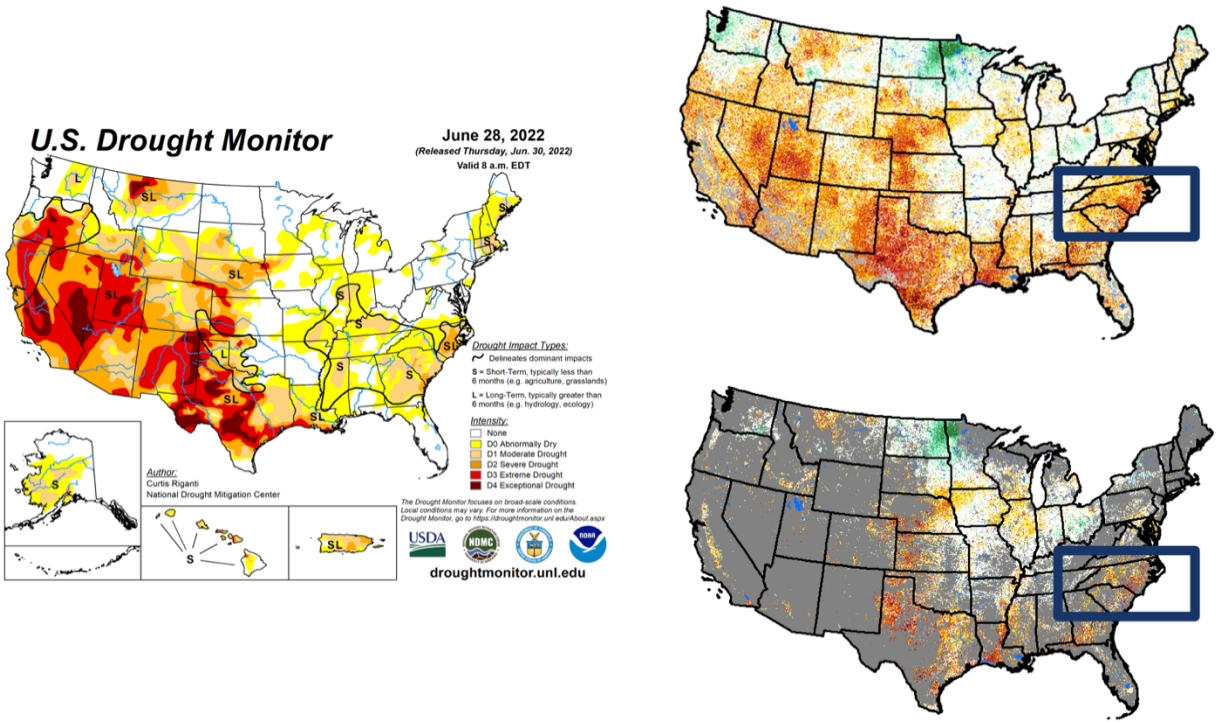

Figure S4: (left) The US Drought Monitor map for the week of 22–28 June 2022 (https://droughtmonitor.unl.edu); and Vegetation Drought Response Index (VegDRI, https://vegdri.unl.edu), at 1 km^2 spatial resolution for the week of 20–26 June 2022, for (upper right) all land cover types and (lower right) croplands only. Conditions for the following week look similar. VegDRI is one of the many pieces of data the US Drought Monitor authors use to develop their maps. The development of VegDRI involves satellite observations of vegetation types and conditions, as well as soil characteristics and climate data. The focused area in the irrigation case study is indicated by dark-blue boxes in the right panels that was suffering from short- and long-term droughts according to the US Drought Monitor. Maps were last retrieved on 12 July 2024.

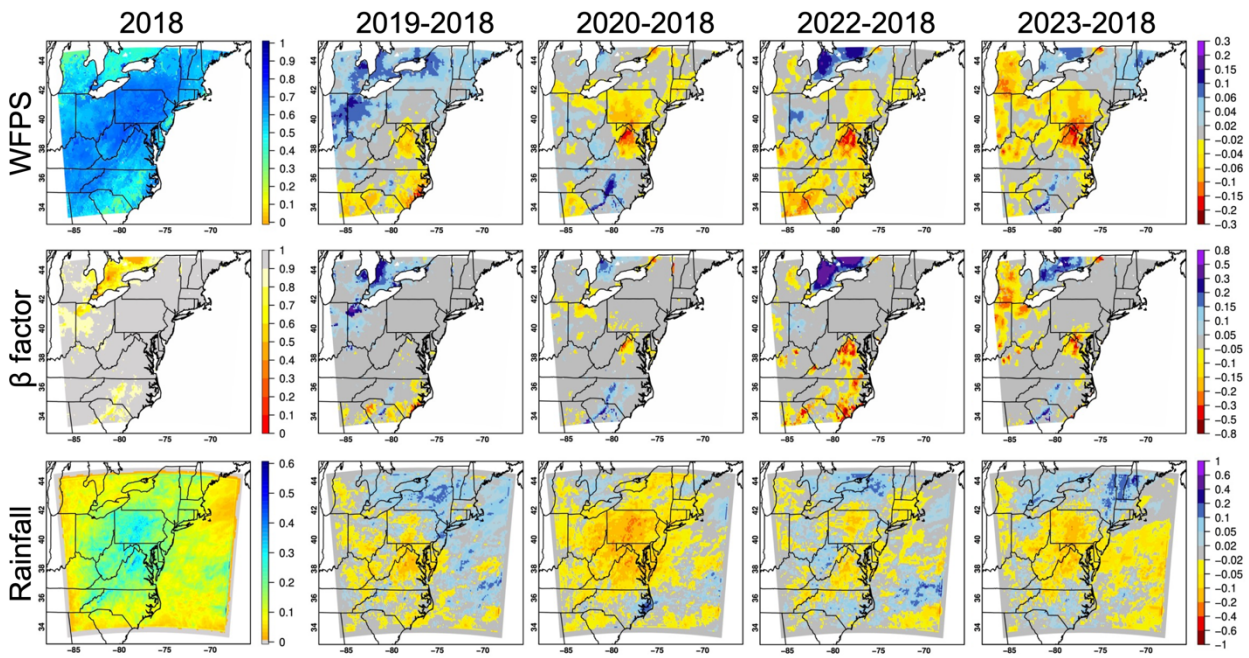

Figure S5: MJJ (upper) water-filled pore space θ; (middle) daytime SM factor controlling stomatal resistance (β) factor (CLM type); and (lower) rainfall and their interannual differences (mm h^{-1}) from WRF-Chem's baseline simulation. θ is relevant to soil NO and HONO emission modeling and β is a crucial parameter in modeling multiple processes including photosynthesis, photosynthesis-based dry deposition rates, and biogenic isoprene emissions. Rainfall strongly impacts wet deposition modeling and indirectly impacts dry deposition and biogenic emission modeling.

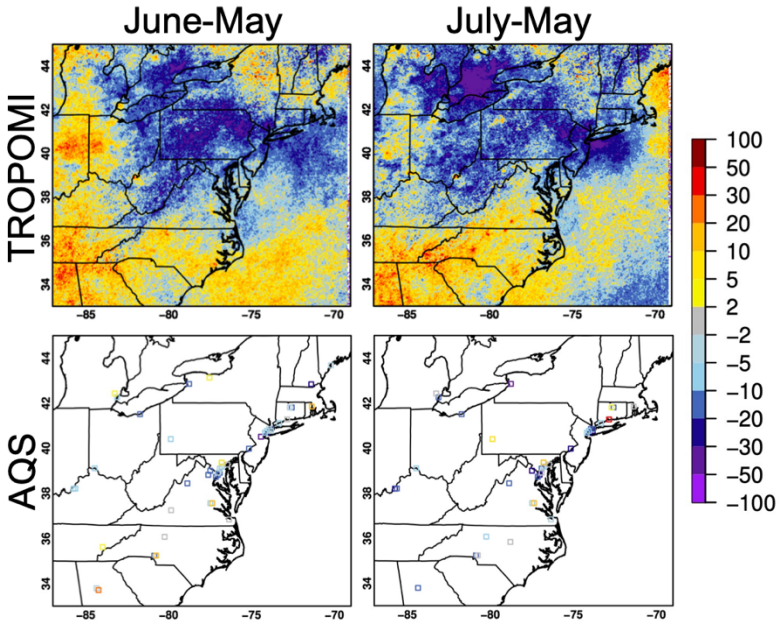

Figure S6: Relative differences (%) of multi-year monthly-mean (upper) TROPOMI NO_2 columns and (lower) AQS 19 UTC surface NO_2 concentrations. Observations from the AQS sites having <10% missing data were used. Note that AQS NO_2 has a strong focus on urban/suburban areas. WRF-Chem results indicate qualitatively similar spatially varying (intra)seasonal variability in surface and column NO_2.

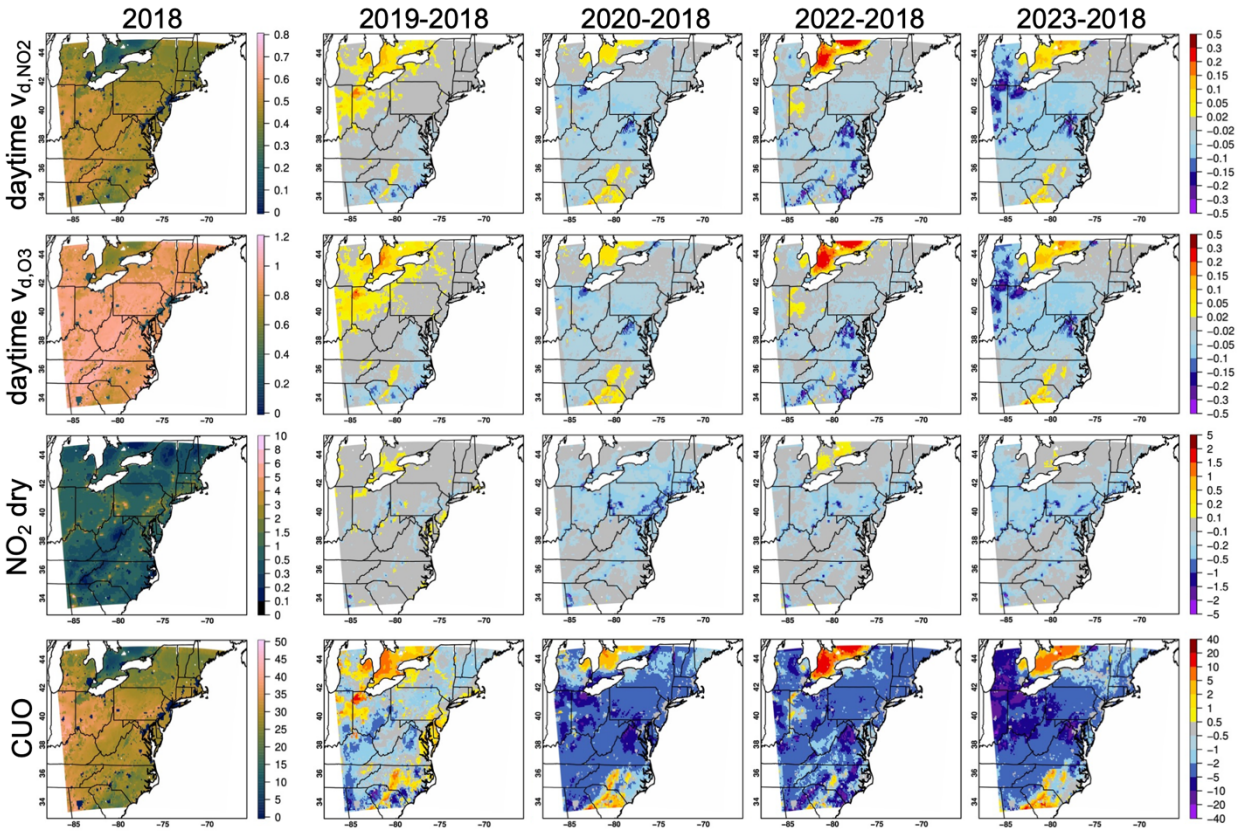

Figure S7: WRF-Chem MJJ daytime-average NO_2 and O_3 dry deposition velocities (v_d, cm s^{-1}), as well as NO_2 dry deposition mass fluxes (kgN ha^{-1} a^{-1}) and cumulative O_3 stomatal uptake (CUO, mmol m^{-2}). Results are averaged or integrated for MJJ and the interannual differences are indicated. At Harvard Forest, WRF-Chem MJJ $v_{d,o3}$ and measured $v_{d,o3}$ (during 1990–2000 June-July-August-September, Clifton et al., 2017) display similar diurnal cycles, with their daytime maxima and nighttime minima of 0.8–1.0 and <0.3 cm s^{-1}, respectively.

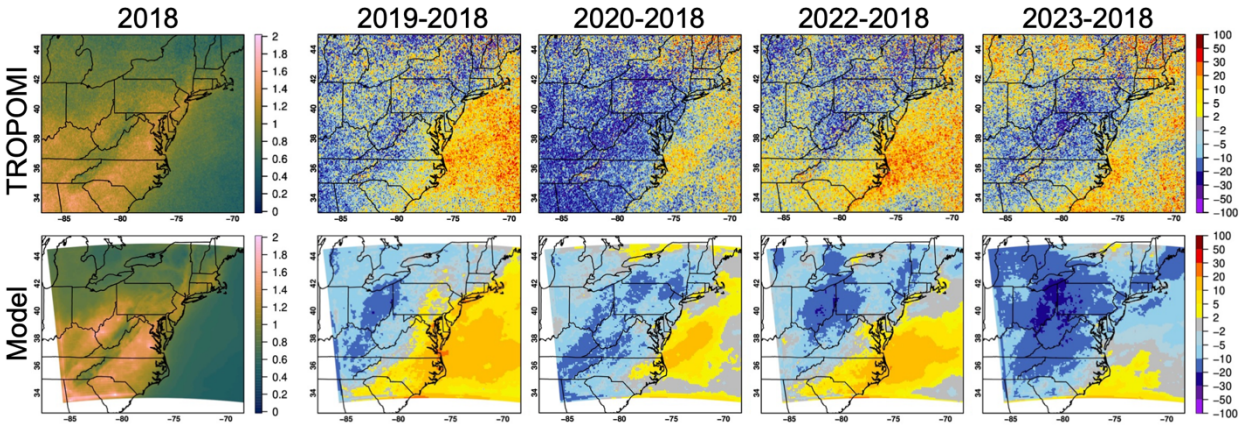

Figure S8: (Upper) TROPOMI and (lower) WRF-Chem HCHO columns. Results are averaged for MJJ 2018 (left, in $\times 10^{16}$ molec. cm^{-2}) and shown together with the % differences between MJJ of each of the following years and 2018.

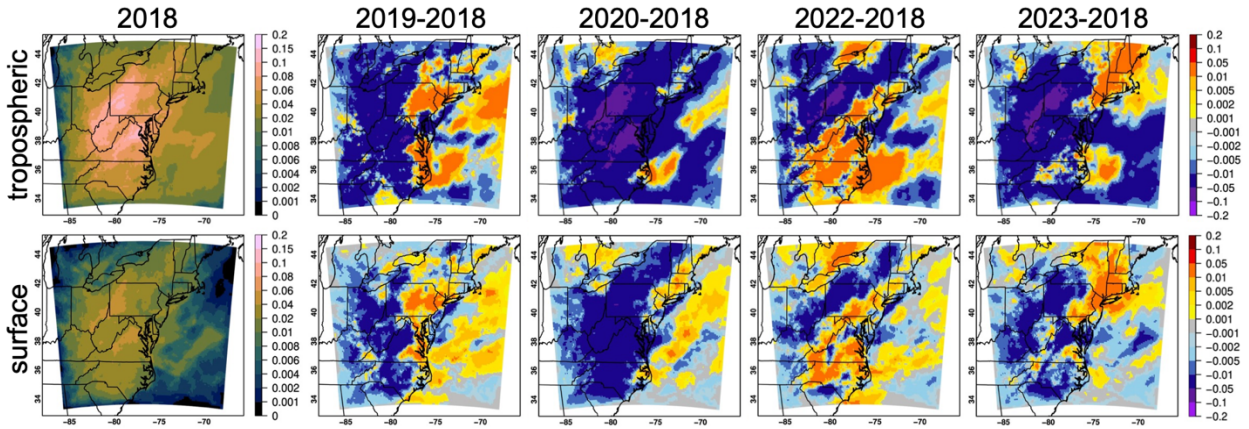

Figure S9: WRF-Chem lightning NO tracer results in ppbv, averaged for 19 UTC of MJJ 2018 and the interannual differences are indicated. Upper and lower panels show tropospheric-column average and surface-level conditions, respectively.

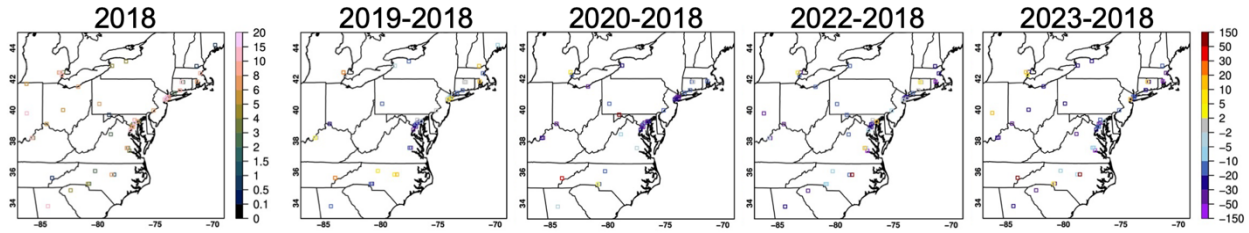

Figure S10: AQS 19 UTC surface NO_2 concentrations. Results are averaged for MJJ 2018 (left, in ppbv), shown together with the % differences between MJJ of each of the following years and 2018. Observations from the AQS sites having <10% missing data for each year were used. Daytime-averaged AQS surface NO_2 indicates qualitatively similar year-to-year changes (not shown).

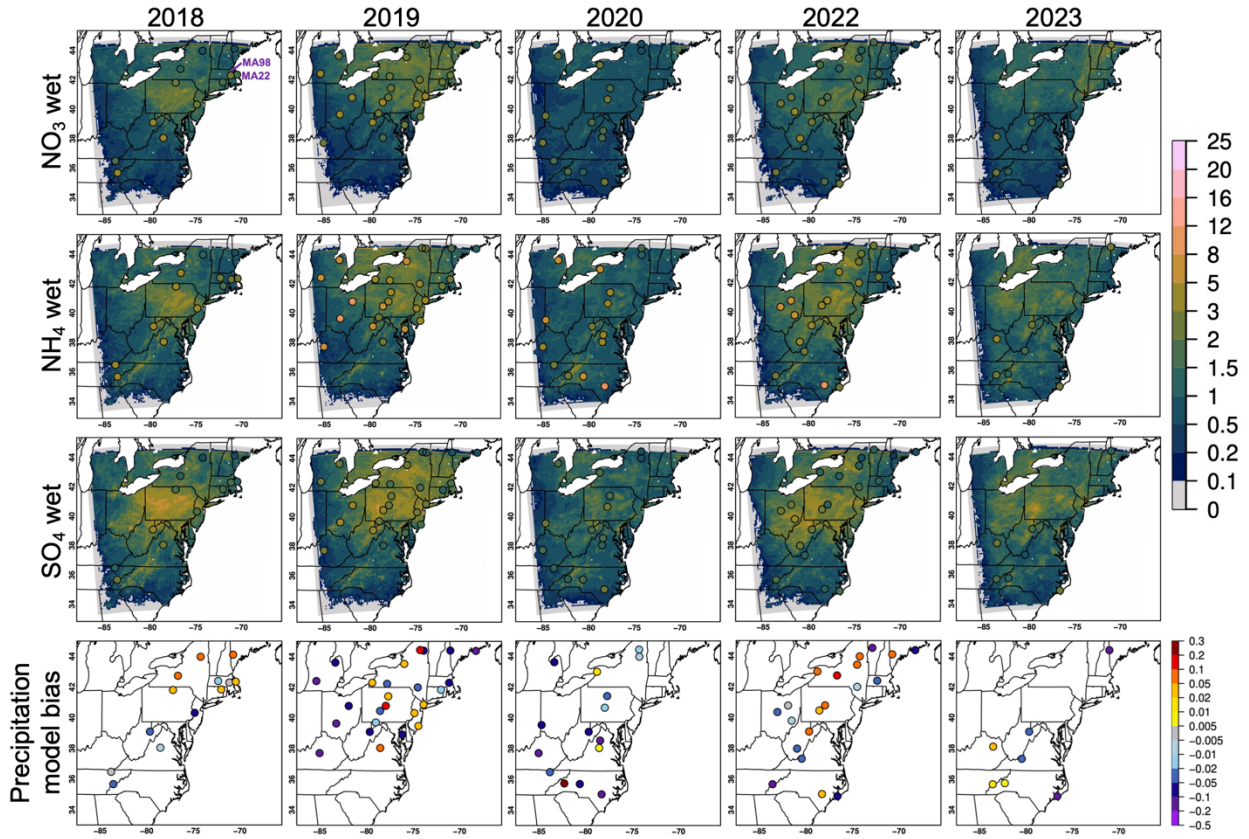

Figure S11: WRF-Chem modeled NO_3 (HNO_3+pNO_3), NH_4 (NH_3+pNH_4), and SO_4 (SO_2+pSO_4) wet deposition fluxes (kgN or kgS ha^{-1} a^{-1}) overland for MJJ 2018–2023, with observations from the NADP/NTN network overlaid in circles. Modeled precipitation biases (mm h^{-1}) are indicated in the bottom panels. Modeled rainfall rate maps are shown in Fig. S5. The evaluation of these fluxes is only performed for sites with <10% missing/invalid chemical data and the statistics are summarized in Table S2. Note that in the 2018 maps, for enhanced readability, data for site MA22 are plotted slightly away from the actual site location (42.3501°N, 71.1044°W) which is very close to site MA98 (42.2953°N, 71.134°W).

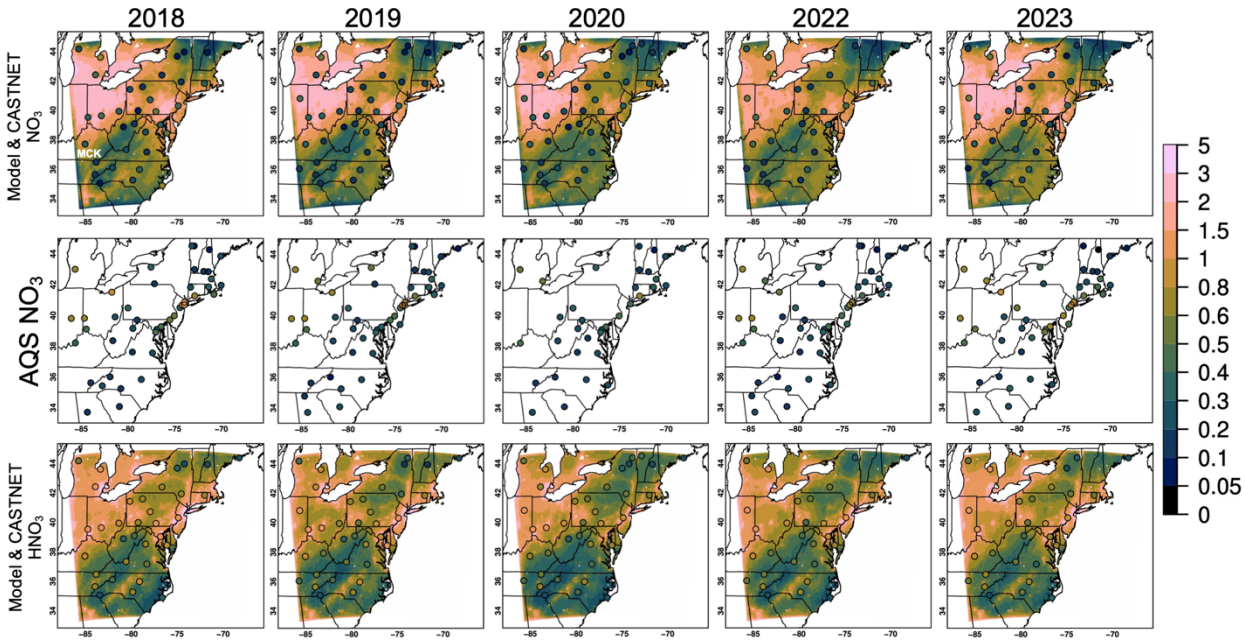

Figure S12: Modeled surface NO_3 aerosols and HNO_3 (all in μg m^{-3}) overland for MJJ 2018–2023, with observations from the CASTNET network overlaid in circles. The evaluation of these fluxes is only performed for sites with <10% missing/invalid data and the statistics are summarized in Table S2. AQS surface fine NO_3 observations, available every ~3 days are shown in the middle row. Observations from collocated CASTNET sites MCK131 and MCK231 (location marked in white in the upper left panel) are averaged for the plots.

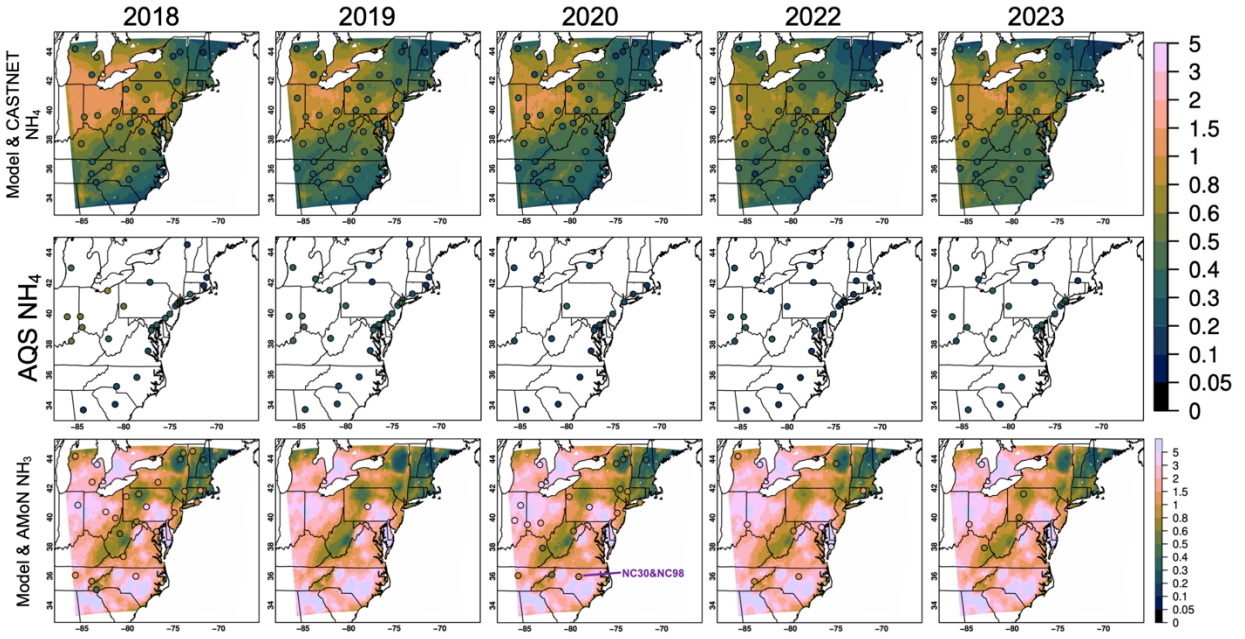

Figure S13: Modeled surface NH_4 aerosols and NH_3 (all in μg m^{-3}) overland for MJJ 2018–2023, with observations from the surface networks overlaid in circles. The evaluation is only performed for sites with <10% missing/invalid data and the statistics are summarized in Table S2. AQS surface fine NH_4 observations, available every ~3 days are shown in the middle row. Observations from collocated CASTNET sites MCK131 and MCK231 are averaged for the plots. Observations from two AMoN sites NC30 and NC98 (location marked in purple in the bottom row) that fall within the same model grid are averaged for the 2020 NH_3 plot.

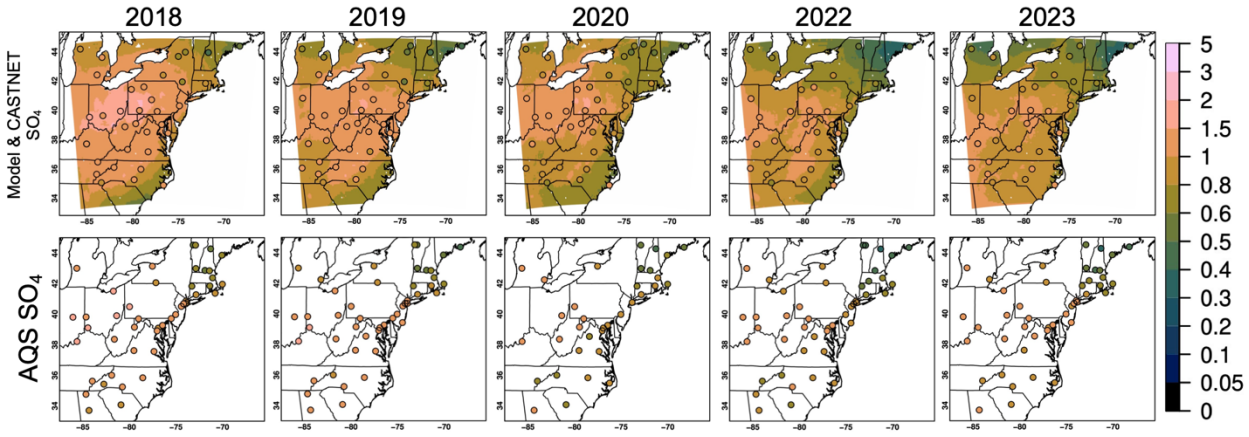

Figure S14: Modeled surface SO_4 aerosols (all in μg m^{-3}) overland for MJJ 2018–2023, with observations from the CASTNET network overlaid in circles. The evaluation is only performed for sites with <10% missing/invalid data and the statistics are summarized in Table S2. AQS surface fine SO_4 observations, available every ~3 days are also shown in the middle row. Observations from collocated CASTNET sites MCK131 and MCK231 are averaged for the plots.

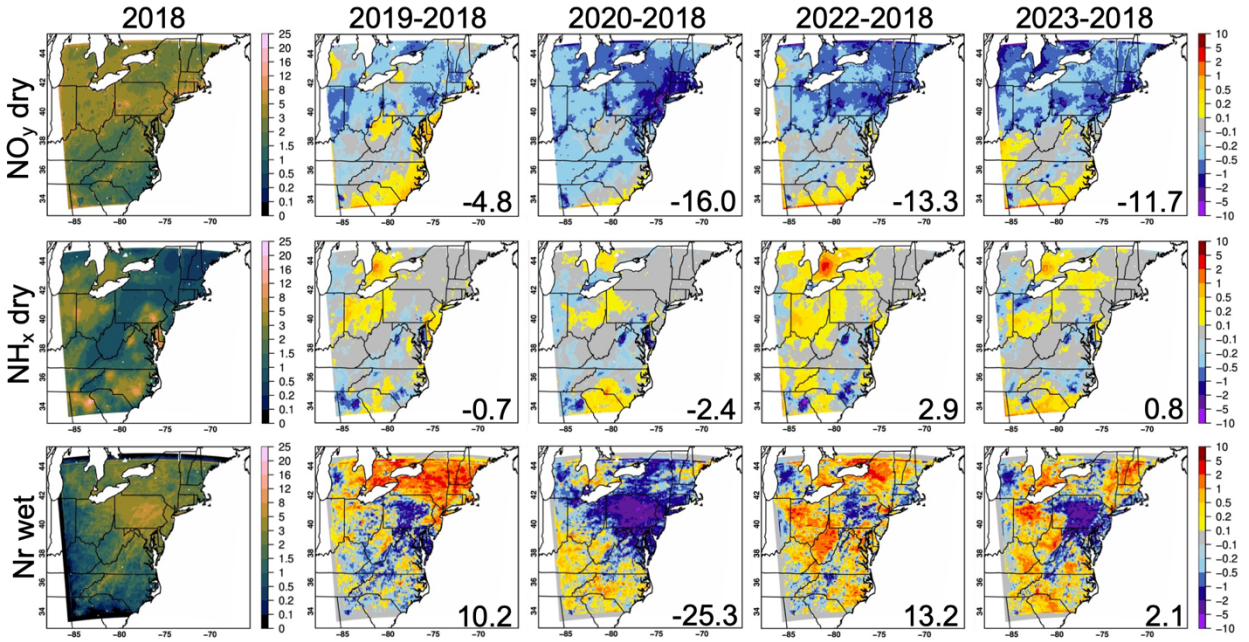

Figure S15: WRF-Chem 2018 MJJ (upper) NO_y dry deposition; (middle) NH_x dry deposition; and (lower) Nr wet deposition fluxes overland and the differences between MJJ of each of the following years and 2018, all in kgN ha^{-1} a^{-1}. Numbers at the corners of the difference plots indicate the % changes relative to MJJ 2018.

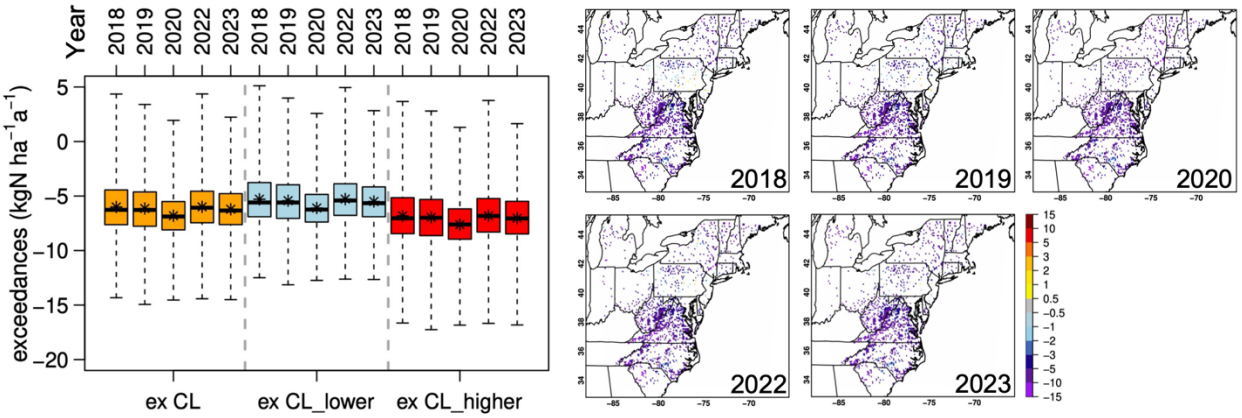

Figure S16: Box-and-Whisker plots and maps of the critical load (CL) exceedances in kgN ha^{-1} a^{-1}. CL exceedances are estimated by comparing the modeled MJJ 2018–2023 Nr deposition fluxes and the CL thresholds as well as the lower (precautionary) and higher (benefit-of-doubt) limits of the 95% confidence interval of these CL thresholds for herbaceous plants in Simkin et al. (2016). Spatially varying biases in the modeled NH_4+NO_3 wet deposition fluxes (Fig. S11) should be accounted for when interpreting these plots.

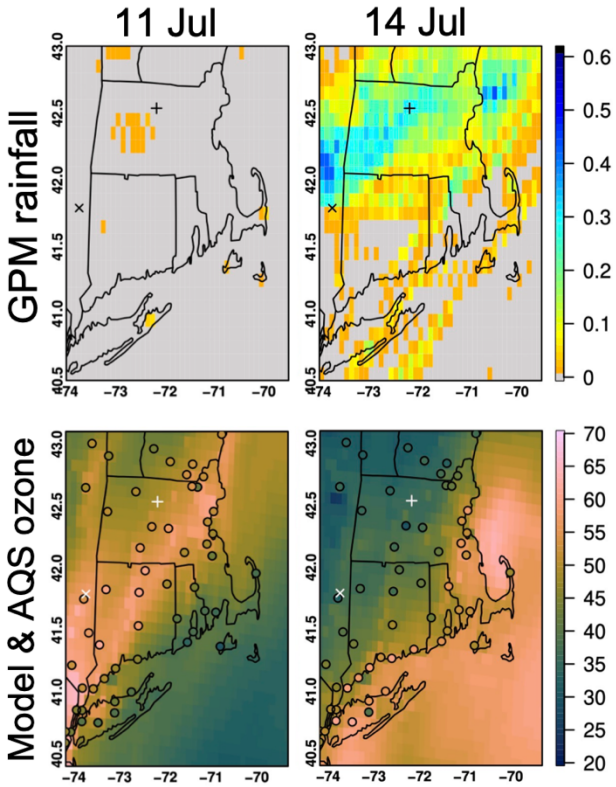

Figure S17: (Upper) GPM/IMERG daily rainfall (mm h^{-1}) on 11 and 14 July 2022. Daily-average rainfall rates measured at the Harvard Forest and the CRN-Millbrook site are both 0 mm h^{-1} on 11 July 2022 and 0.450 and 0.175 mm h^{-1} on 14 July 2022, respectively (data last retrieved from: https://harvardforest1.fas.harvard.edu/exist/apps/datasets/showData.html?id=HF001; and https://www.ncei.noaa.gov/access/crn/sensors.htm?siteId=1118 on 6 February 2024); (lower) AQS surface daytime O_3 observations on 11 and 14 July 2022 for sites having <10% missing data, overlaid on O_3 fields from WRF-Chem with SMAP DA enabled, depicting sharp O_3 decreases in and around Massachusetts soon after the precipitation event occurring ~14 July 2022.

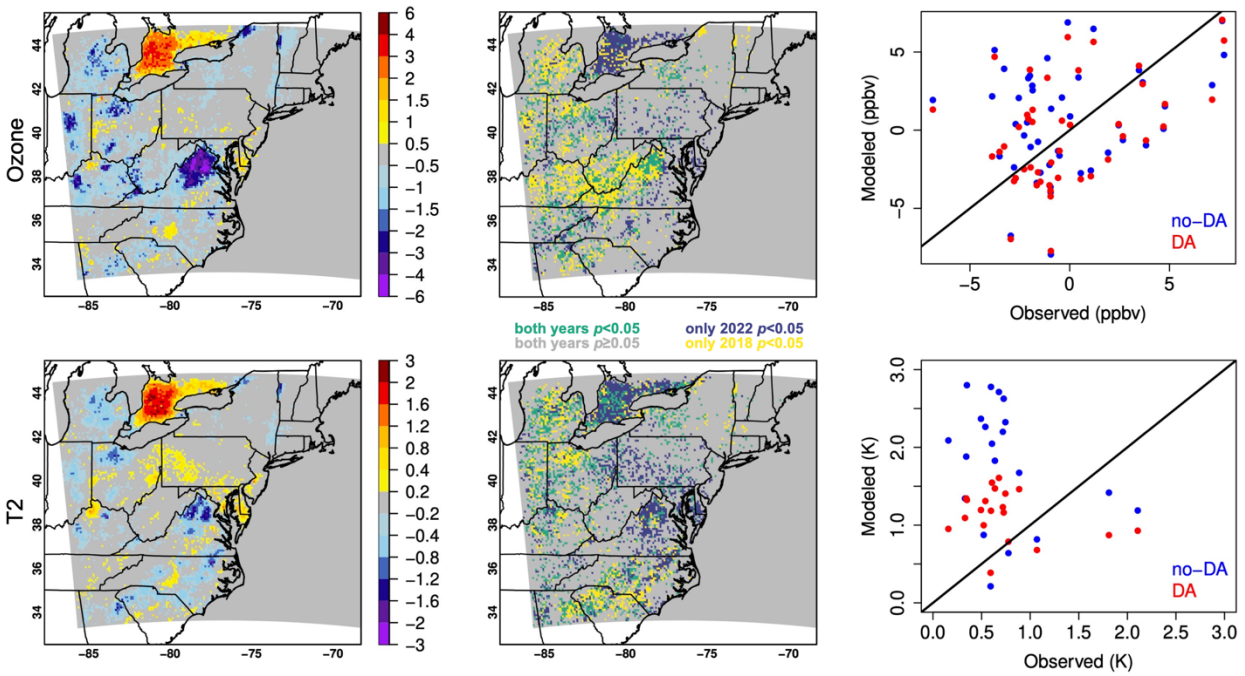

Figure S18: (left) Impacts of SMAP data assimilation (DA) on July 2022-July 2018 monthly daytime surface O_3 (ppbv) and air temperature (K) differences, i.e., Figs. 14i-14h and 14l-14k; (middle) the *p* values of Student's *t*-tests that compare no-DA and DA daytime surface O_3 and air temperature in July 2022 and July 2018 in all model grids; and (right) scatterplots of the modeled (no-DA and DA) vs. observed daytime surface O_3 and air temperature interannual differences in/near northern Virginia (38–40°N; 77–80°W). The improvement in surface air temperature interannual differences (by up to 1.6 K) due to the SMAP DA favorably impacted the model's O_3 performance in northern Virginia. The improvements in other key meteorological fields due to the DA, which may be relatively smaller than that in air temperature according to previous studies (e.g., Huang et al., 2021, 2022), also impacted the model's O_3 performance.

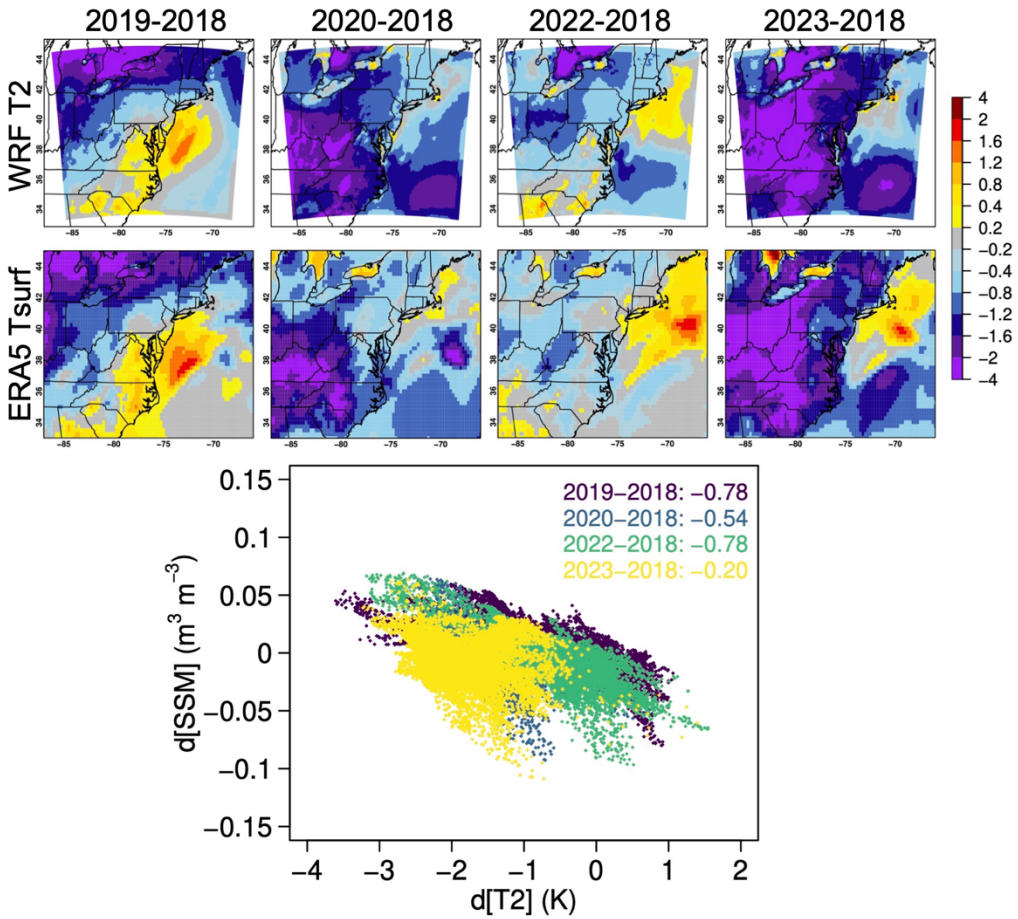

Figure S19: Interannual differences in (upper) WRF daytime 2 m air temperature (T2) and (middle) ERA5 surface air temperature fields in K. The lower panel scatterplot indicates how strong the interannual differences in the modeled surface soil moisture (SSM) influenced the surface air temperature dynamics overland, with their correlation coefficients (p<<0.01) shown in the upper-right legend.

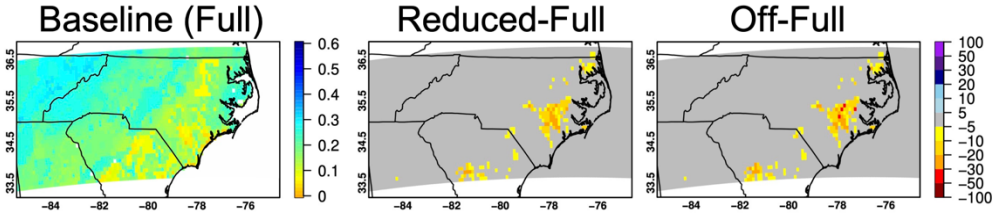

Figure S20: (Left) Noah-MP column-averaged soil moisture (m^3 m^{-3}) over the stressed croplands in the Carolinas, in early mornings of 21–30 June 2022, as well as its % changes in response to adjustments in irrigation schemes.

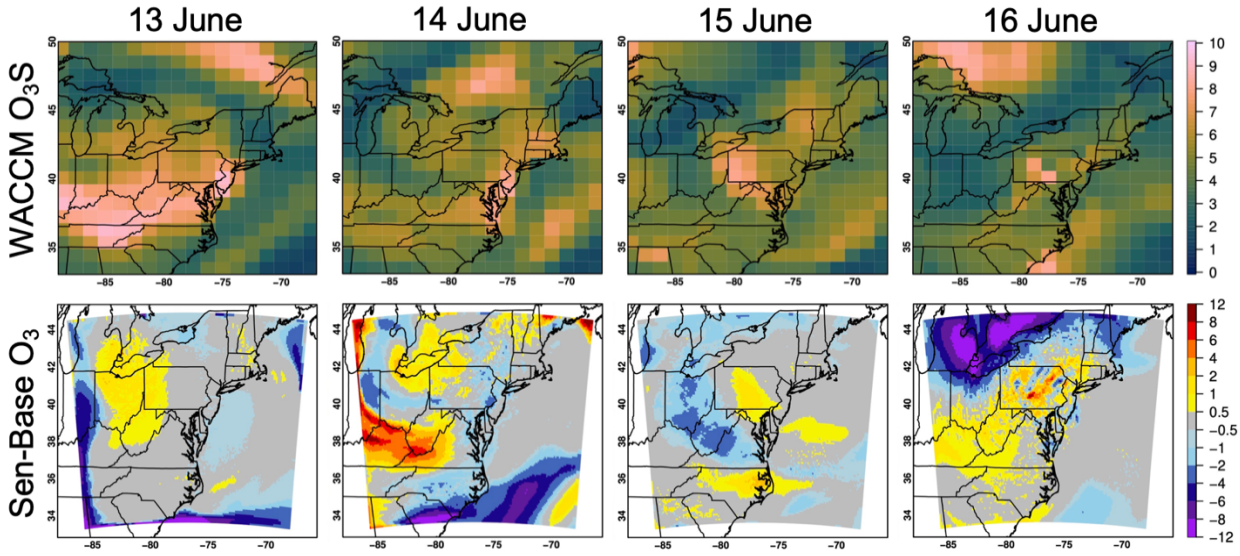

Figure S21: (upper) Stratospheric influences on surface O_3 at 18 UTC of 13–16 June 2023 (in ppbv), based on baseline WRF-Chem simulation's chemical boundary condition model WACCM's stratospheric O_3 tracer; and (lower) daytime surface O_3 sensitivities to perturbations in chemical boundary conditions for the same days, where "Sen" refers to WRF-Chem simulation using chemical boundary conditions from WACCM with the FINN fire emission input. Units are all in ppbv. WRF-Chem "Sen" vs. AQS daytime O_3 RMSEs (ppbv) for 13–16 June 2023 are 7.0, 7.1, 7.6, and 7.0 ppbv, respectively.

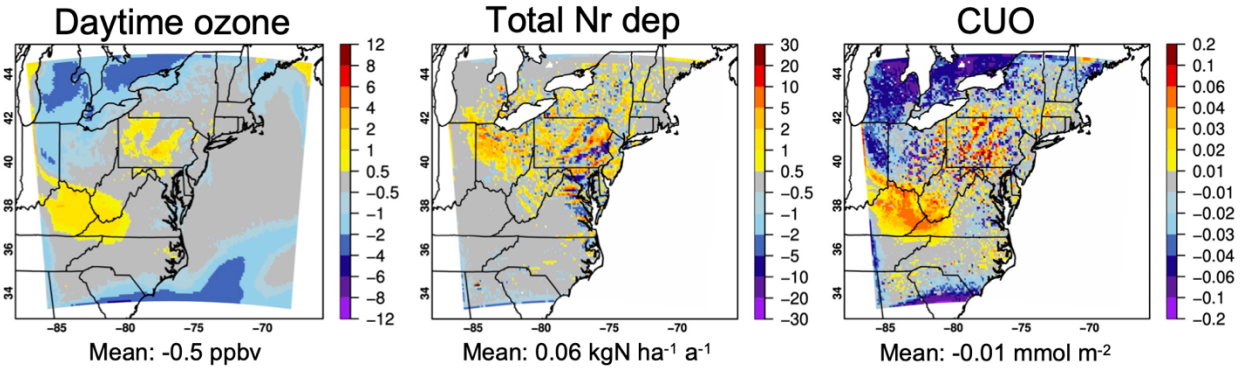

Figure S22: Differences in (left) daytime surface O_3 concentrations (ppbv); (middle) total Nr deposition overland (kgN ha^{-1} a^{-1}); and (right) period-cumulated O_3 stomatal uptake (mmol m^{-2}) between the "Sen" and baseline WRF-Chem simulations, averaged for 13–16 June 2023. "Sen" refers to WRF-Chem simulation using chemical boundary conditions from WACCM with the FINN fire emission input. Domain-wide mean values are indicated at the bottom of each panel.

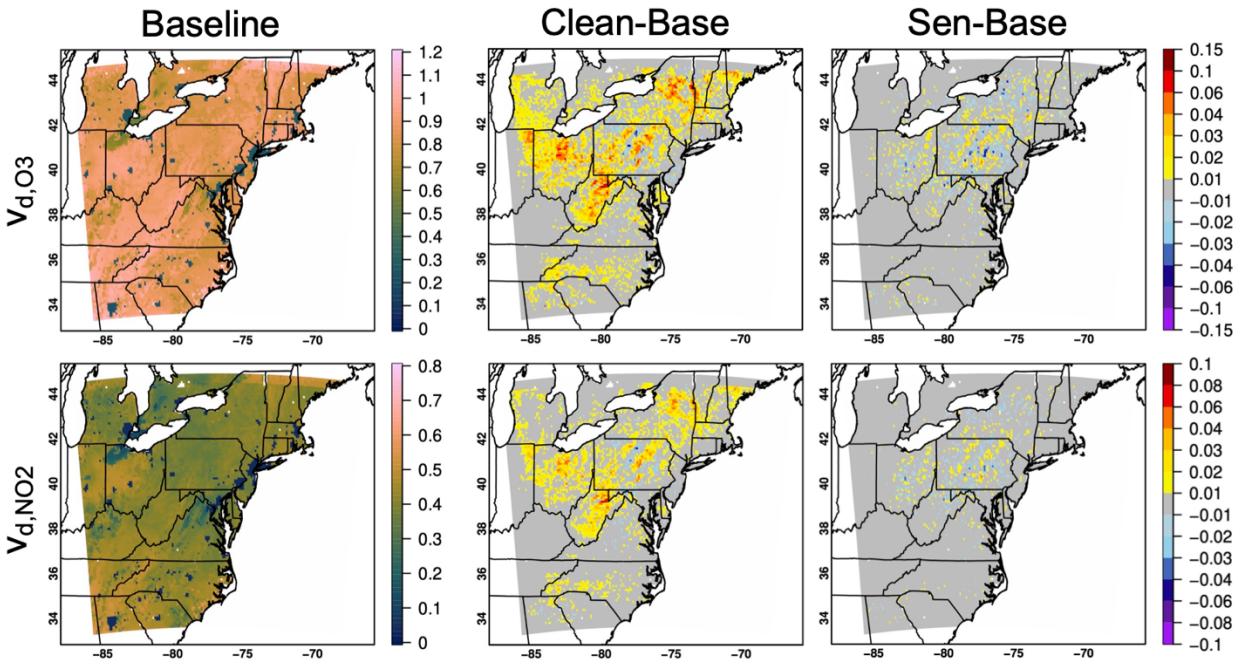

Figure S23: Daytime O_3 and NO_2 dry deposition velocities (cm s^{-1}), averaged for 13–16 June 2023 from the baseline WRF-Chem simulation and their sensitivities to perturbations in chemical boundary conditions. "Clean" and "Sen" refer to WRF-Chem simulations using clean and an alternative WACCM (with the FINN fire emission input) chemical boundary conditions, respectively.

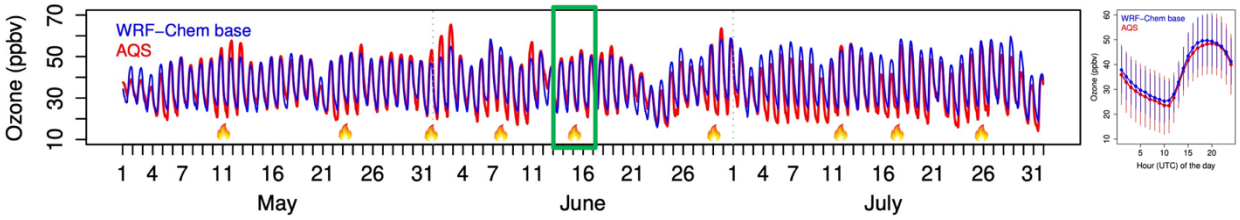

Figure S24: (left) Timeseries of the domain-mean observed and WRF-Chem modeled hourly surface O_3 in MJJ 2023 at AQS sites. Canadian wildfire impacted events are marked by signs of fire. Green box denotes the 13–16 June 2023 period discussed in Section 3.3.3; and (right) observed and WRF-Chem modeled mean and standard deviation of MJJ 2023 surface O_3 at different hours of the day.

References (not cited in the manuscript)

Clifton, O. E., Fiore, A. M., Munger, J. W., Malyshev, S., Horowitz, L. W., Shevliakova, E., Paulot, F., Murray, L. T., and Griffin, K. L.: Interannual variability in ozone removal by a temperate deciduous forest, Geophys. Res. Lett., 44, 542–552, https://doi.org/10.1002/2016GL070923, 2017.

Hand, J. L., Prenni, A. J., and Schichtel, B. A.: Trends in seasonal mean speciated aerosol composition in remote areas of the United States from 2000 through 2021, J. Geophys. Res. Atmos., 129, e2023JD039902, https://doi. org/10.1029/2023JD039902, 2024.